Tunable d-Band Centers of Ni_5P_4 Ultra-Thin Nanosheets for Highly-Efficient Hydrogen Evolution Reaction

Chengcheng Miao, Yanmei Zang, Hang Wang, Xinming Zhuang, Ning Han, Yanxue Yin, Yandong Ma,* Ming Chen, Ying Dai, SenPo Yip, Johnny C. Ho,* and Zai-xing Yang*

Although the recent advance of ultra-thin 2D nanosheets for hydrogen evolution reaction (HER) is remarkable, there are still substantial challenges to reliably control their physioelectric and electrochemical properties to employ as highly-efficient electrocatalysts. Herein, based on complementary theoretical and experimental studies, the d-band center position of ultra-thin 2D Ni_5P_4 nanosheets can be manipulated by simple heteroatom doping. Interestingly, the Fe-doped nanosheets yield the lowest d-band center position, but they do not display the optimal Gibbs free energy of adsorbed H atoms due to the imbalance of adsorption and desorption of adsorbed H atoms. With the proper Co doping (i.e., 20%), the nanosheets exhibit the best electrocatalytic performance along with an excellent stability. The overpotential is only 100.5 mV at 10 mA cm^{-2} with a Tafel slope of 65.8 mV dec^{-1}, which is superior than those of Fe-doped, Cu-doped, and pristine Ni_5P_4 nanosheets. Ultraviolet photoelectron and X-ray photoelectron spectroscopy further verify the downshift of d-band centers of nanosheets by optimal doping, illustrating that Ni with the lower binding energy mainly dominates the active sites. All these results provide a valuable design scheme of dopants to control the d-band center position of nanosheets for next-generation highly-efficient HER electrocatalysts.

1. Introduction

In the past decades, the increasing global energy demand and associated environmental pollution problems have driven the urgent search for clean and sustainable energy fuels. Among many candidates, the green hydrogen generated by electrochemical water splitting is widely considered as one of the promising fuels to resolve the issues.[1–3] Substantial investigations are then focused on establishing high-performance and cost-effective electrochemical hydrogen generation schemes powered by renewable energy sources. Although there are lots of recent advances in hydrogen evolution reaction (HER), Pt-based noble metal electrocatalysts are always demonstrated with the excellent electrocatalytic activity, but the scarcity of Pt would inevitably hinder its practical utilization. Therefore, it is urgently required to develop highly-active and low-cost non-noble electrocatalysts as alternatives in order to sustain the future technology development.[4–9]

Recently, owing to the abundant positive charge of $Ni^{\delta+}$, the non-noble transition metal phosphide of Ni_5P_4 has been revealed as a promising alternative candidate for next-generation highly-efficient HER electrocatalyst.[10,11] Until now, different strategies including the enhancement of active-site concentration,[12–15] the reduction of charge transfer resistance (R_{ct})[16,17] and the optimal control of morphology[12,13] have been attempted to further improve the electrocatalytic characteristics of Ni_5P_4. For instance, with the unique geometry and the large specific surface area, 2D ultrathin nanosheet electrocatalysts are usually found to exhibit the exceptional HER performance, which is benefited from their abundant active sites, minimized R_{ct} as well as facilitated pathways of electrolyte diffusion and gas release.[12,18,19] At the same time, it has been reported that the direct tuning of d-band center of transition metals can modify the adsorption energy between valence states of adsorbates and d-states of transition metals, and then optimize the Gibbs free energy of adsorbed H atoms (G_H), contributing to the enriched HER activity and the significantly enhanced performance.[20,21] Technically, the doping of heteroatoms with different electronegativity is an effective way to modulate the d-band center of transition metals.[22,23] In the recent literature reports, Co, Fe, and Cu doping have been illustrated to successfully optimize

C. Miao, Y. Zang, X. Zhuang, Y. Yin, Y. Ma, M. Chen, Y. Dai, Z.-x. Yang
School of Physics
State Key Laboratory of Crystal Materials
School of Microelectronics
Shandong University
Jinan 250100, P. R. China
E-mail: yandong.ma@sdu.edu.cn; zaixyang@sdu.edu.cn

H. Wang, N. Han
State Key Laboratory of Multiphase Complex Systems
Institute of Process Engineering
Chinese Academy of Sciences
Beijing 100190, P. R. China

S. P. Yip, J. C. Ho
Institute for Materials Chemistry and Engineering
Kyushu University
Fukuoka 816-8580, Japan

J. C. Ho
Department of Materials Science and Engineering
City University of Hong Kong
Hong Kong 999077, P. R. China
E-mail: johnnyho@cityu.edu.hk

The ORCID identification number(s) for the author(s) of this article can be found under https://doi.org/10.1002/admi.202200739.

ADVANCED
SCIENCE NEWS
www.advancedsciencenews.com

ADVANCED
MATERIALS
INTERFACES
www.advmatinterfaces.de

the position of d-band centers of the host catalysts, resulting in the higher electrocatalytic efficiency for HER.[24,25] In particular, Wang et al. found that the d-band center of Mo_2C nanoparticles can be downshifted by the optimal doping of Co, which decreases the quantity of filling state of electrons in antibonding orbitals, resulting in the optimized G_H by weakening the interaction between adsorbates and catalyst surfaces. In this case, with a good balanced adsorption and desorption of adsorbed H atoms (H), an improved HER performance can be observed.[24] This specific phenomenon has also been observed in Cu-doped Ni porous networks[25] and Fe-doped Co_2P nanorods,[26] where the proper doping can facilitate the HER performance of the host catalysts by the downshifting of d-band centers. However, it still lacks of the systematic investigation about the tuning of d-band centers of ultrathin 2D nanosheets by controlled doping of different heteroatoms for enhanced HER characteristics.

In this work, the controlled doping of Co, Fe, and Cu is demonstrated to effectively modulate the position of d-band centers of ultra-thin Ni_5P_4 nanosheets. These heteroatom-doped ultra-thin nanosheets with tunable d-band centers are prepared by a solvothermal method, followed by a chemical vapor deposition (CVD) phosphorization process. In short, nickel hydroxide with nanosheet morphology is prepared first by a solvothermal method, as reported in the previous literature.[27] After the success growth of precursor, the phosphating process is completed by using NaH_2PO_2 as phosphorus source during a typical CVD process. PH_3 gas is generated by the decomposition of NaH_2PO_2 and reacts with nickel hydroxide to form the expected Ni_5P_4-based nanosheets.[28] Based on the density functional theory (DFT) simulation, the Fe-doped nanosheets have the largest magnitude of the d-band center downward shift as compared to those of the Fe-doped and Co-doped nanosheets. However, the ΔG_H value of Co-doped nanosheets is the one closest to 0 eV among all heteroatom-doped nanosheets. This observation can be due to the appropriate d-band center positioning of Co-doped nanosheets, which leads to the balanced adsorption and desorption of H by tuning the number of filling state of electrons in antibonding orbitals. This way, with the lowest absolute value of ΔG_H, the ultra-thin Co-doped Ni_5P_4 nanosheets display the best HER characteristics with an impressively small overpotential of 176.8 mV at 100 mA cm^{-2} and a Tafel slope of 65.8 mV dec^{-1} in 1.0 M KOH. This outstanding HER performance is attributable to the proper downshift of d-band centers and the optimized ΔG_H value of nanosheets. This heteroatom doping strategy presents a simple but effective way to manipulate the d-band centers and ΔG_H values of ultra-thin 2D nanosheets, being also applicable to other transition metal based nanostructures for further enhanced HER processes.

2. Results and Discussion

The DFT simulation is first employed to predict the tunable d-band center position of Ni_5P_4 by doping with different heteroatoms. The theoretical calculation is processed based on the atomic models depicted in **Figure 1**a, in which the dopants of Co, Fe, and Cu atoms are energetically favorable to replace the Ni atoms of Ni_5P_4. The d-band density of state (DOS) plots of all electrocatalysts are shown in Figure 1b. Compared to pristine Ni_5P_4 (–1.71 eV), a downward shift of the d-band center is observed in 10% Co-doped Ni_5P_4 (–1.78 eV), 20% Co-doped Ni_5P_4 (–1.80 eV), and 30% Co-doped Ni_5P_4 (–1.77 eV). Similar d-band center tuning trends can be observed in 20% Cu-doped Ni_5P_4 and 10% Fe-doped Ni_5P_4, which exhibit d-band centers of –1.78 and –1.84 eV, respectively. Obviously, the d-band center of Ni_5P_4 can be tuned simply by changing doping heteroatoms and doping amounts. The downward shifting of d-band center tends to weaken the bonding strength between transition-metal d states and H (Figure 1c), resulting in the change of hydrogen adsorption and desorption processes.[20] This effect would lead to the change of ΔG_H and in turn affects the electrocatalytic performance. Furthermore, to verify the intrinsic effect of dopants (Co/Fe/Cu) on HER, the ΔG_H values of pristine Ni_5P_4 and Co/Fe/Cu-doped Ni_5P_4 are calculated and compiled in Figure 1d. Compared to the ΔG_H of pristine Ni_5P_4 (–0.34 eV), 10% Co-doped Ni_5P_4, 20% Co-doped Ni_5P_4, 30% Co-doped Ni_5P_4, 20% Cu-doped Ni_5P_4, and 10% Fe-doped Ni_5P_4 exhibit closer to the thermoneutral values of 0.3, –0.12, 0.2, 0.25, and 0.15 eV, respectively. Notably, although 10% Fe-doped Ni_5P_4 nanosheet has the smallest value of d-band center, it does not possess the optimal ΔG_H. It is because an appropriate d-band center (neither too high nor too low) can possess a near-optimal binding energy of H and the corresponding alkaline HER activity, which is conformed to a volcano-type relationship via Sabatier principle.[29] Hence, it should be careful for the design or selection of dopants in the d-band center control for the next-generation highly-efficient HER electrocatalysts.

To verify the theoretical prediction of DFT simulation, the electrochemical performance of the as-prepared Ni_5P_4-based nanosheets is investigated in 1.0 M KOH at room temperature. As the Ni_5P_4-based nanosheets are prepared on carbon cloth (CC) substrates, for comparison, the electrocatalytic activities of Pt wires and bare CC substrates are also tested. As shown in the linear sweep voltammetry (LSV) curves in **Figure 2**a, a nearly horizontal polarization curve is observed in bare CC, indicating its poor activity for alkaline HER, while the Pt wire exhibits an excellent HER activity with a low overpotential of 36.2 mV at a geometric catalytic current density of 10 mA cm^{-2}. Under a current density of 10 and 100 mA cm^{-2}, 20% Co-doped Ni_5P_4 nanosheets yield the overpotentials of 100.5 and 176.8 mV, respectively, which are far lower than those of pristine Ni_5P_4 (193.2 and 443.2 mV). Similar to the Co-doped nanosheets, the electrocatalytic performance improvement are also obtained in 10% Fe-doped Ni_5P_4 nanosheets (160.2 and 247.8 mV) and 20% Cu-doped Ni_5P_4 nanosheets (157.9 and 278.2 mV). In order to study the effect of different doping amounts and different annealing treatment conditions, different doping amounts of Co-doped (10% and 30% doping), Cu-doped (10% and 30% doping), and Fe-doped (5% and 20% doping) nanosheets are shown in Figures S1–S3, Supporting Information, accordingly. Compared to 20% Co-doped Ni_5P_4 nanosheets, 10% and 30% Co-doped Ni_5P_4 nanosheets need higher overpotentials of 159.5 and 139.5 mV at a geometric catalytic current density of 10 mA cm^{-2}, respectively. Similar phenomenon can as well be observed in different doping amounts of Cu-doped and Fe-doped Ni_5P_4 nanosheets. 20% Cu doping and 10% Fe doping are the optimum values for HER performance of Fe-doped and Cu-doped Ni_5P_4 nanosheets, respectively. It is obvious that the
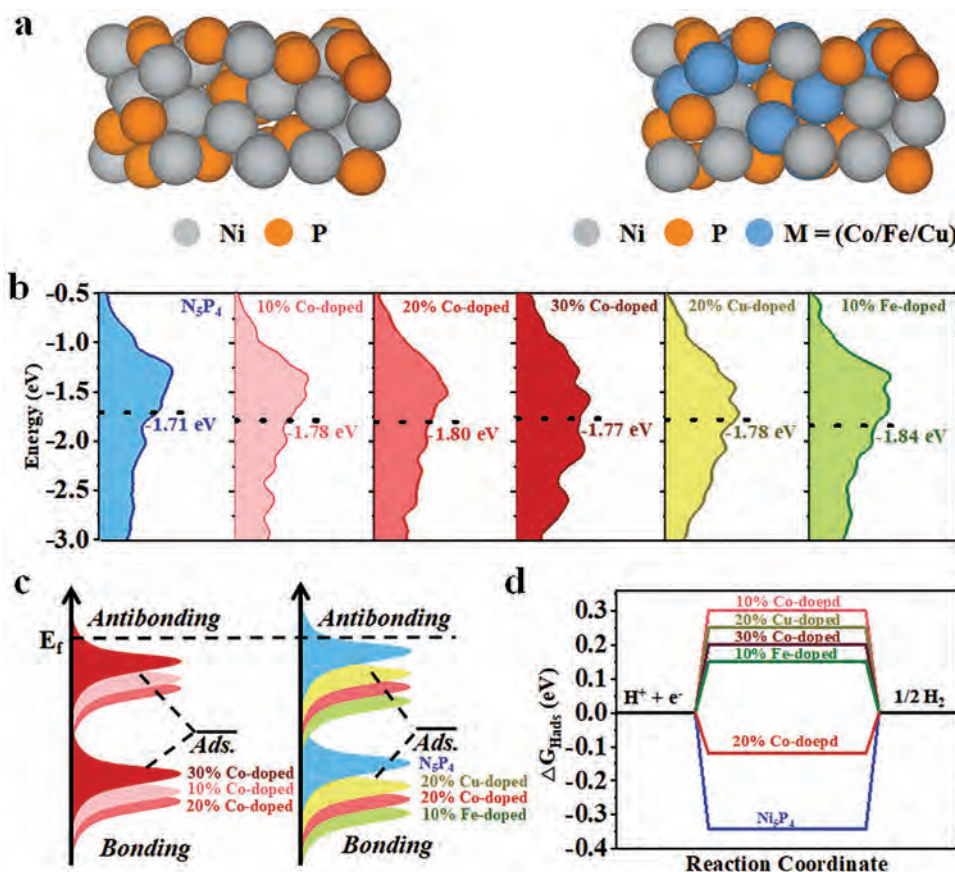
Figure 1. DFT theoretical calculation on the tunable d-band centers of Ni_5P_4 nanosheets. a) The atomic models of Ni_5P_4 and Co/Fe/Cu-doped Ni_5P_4. b) The density of state (DOS) plots of all electrocatalysts. c) The corresponding schematic illustrations of bonding formation between the reaction surface and the adsorbate (Ads.). d) The ΔG_H values of all electrocatalysts.
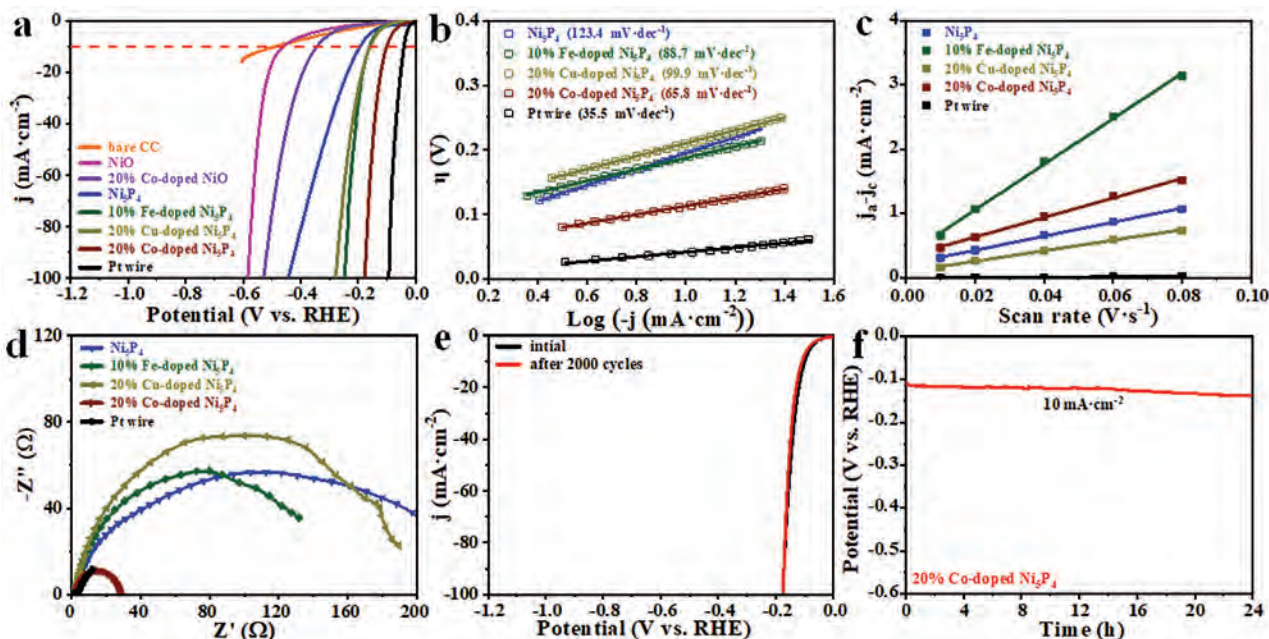
Figure 2. The electrochemical performance of Ni_5P_4 nanosheets with the tunable d-band center in 1.0 M KOH. a) Linear sweep voltammetry curves. b) Tafel plots. c) Double layer capacitances. d) Nyquist plots. e) Linear sweep voltammetry curves of 20% Co-doped Ni_5P_4 before and after cyclic voltammogram scanning for 2000 cycles. f) Stability test of 20% Co-doped Ni_5P_4 at 10 mA cm^{-2} for 24 h.

proper amount of P and the annealing temperature also play an important role on the HER performance of ultra-thin Ni_5P_4 nanosheets. In this case, 20% Co-doped Ni_5P_4 nanosheets annealed with various NaH_2PO_2 amounts and annealing temperatures are shown in Figures S4,S5, Supporting Information, accordingly. The 20% Co-doped Ni_5P_4 nanosheets prepared by using 50 mg of NaH_2PO_2 at an annealing temperature of 300 °C exhibit a lower overpotential than others. Meanwhile, the HER performance of undoped and 20% Co-doped NiO nanosheets are shown in Figure S6, Supporting Information, displaying the higher overpotentials of 342.9 and 460.2 mV in order to achieve a current density of 10 mA cm^{-2}. Furthermore, for further studying the intrinsic activity of the as-prepared electrocatalysts, the LSV curves normalized by electrochemical active surface area (ECSA) is given in Figure S7, Supporting Information, indicating the best intrinsic activity of 20% Co-doped Ni_5P_4 nanosheets compared to others. Furthermore, as shown in Figure S8, Supporting Information, a volcano-type curve is presented between the calculated d-band center and overpotential for all electrocatalysts. The optimal d-band center position is around −1.80 eV, namely, the 20% Co-doped Ni_5P_4 is located closer to the volcano summit. Too low and too high d-band center position are disadvantages for the HER process. The Sabatier principle reveals that the performance of the electrocatalyst is dominated by the balance of the adsorption and desorption energies of adsorbed H atoms.[29]

To shed light on the reaction mechanism of the HER process, Tafel slope is further derived from the LSV curves and presented in Figure 2b. Similar to the previous report,[30] the Pt wire shows the smallest Tafel slope of 35.5 mV dec^{-1}. The calculated Tafel slope of 20% Co-doped Ni_5P_4 nanosheets is 65.8 mV dec^{-1}, which suggests to follow Volmer–Heyrovsky mechanism that the adsorbed H atom couples with another H atom and electron to form H_2.[31] This slope value is smaller than those of 10% Fe-doped Ni_5P_4 (88.7 mV dec^{-1}), 20% Cu-doped Ni_5P_4 (99.9 mV dec^{-1}), and Ni_5P_4 (123.4 mV dec^{-1}) nanosheets. Although this calculated Tafel slope of 20% Co-doped nanosheets is a bit higher than that of the Pt wire, it may still be more conducive to a widespread use in future because of its low cost and environment-friendly nature. Actually, both overpotential and Tafel slope of 20% Co-doped Ni_5P_4 are already superior to the recently reported nickel phosphide-based HER electrocatalysts, such as NiP_2,[32] Fe-doped NiP_2,[33] Se-doped NiP_2,[34] Ni_2P,[35] Mn-doped Ni_2P,[36] Ni_5P_4,[37] Fe-doped Ni_5P_4,[38] and N-doped Ni_5P_4[39] with details shown in **Table 1**. Furthermore, the double-layer capacitance (C_{dl}) derived from the cyclic voltammetry (CV) measurements is considered to further explore the effect of micro-structure properties on HER characteristics. As depicted in Figure 2c, the calculated C_{dl} values of Ni_5P_4, 10% Fe-doped Ni_5P_4, 20% Cu-doped Ni_5P_4, and 20% Co-doped Ni_5P_4 nanosheets are determined to be 5.44, 17.72, 4.09, and 8.09 mF cm^{-2}, respectively. These results indicate that the 20% Co-doped Ni_5P_4 nanosheets presents the relatively larger effective ECSA, designating the more catalytic active sites for the better electrochemical performance.[40]

At the same time, it is also important to explore the interfacial charge transfer kinetics of nanosheets to further explain the enhanced catalytic performance. Electrochemical impedance spectroscopy (EIS) measurements and the corresponding fittings are then carefully performed. Figure 2d shows the

Table 1. Comparison of the electrocatalytic performance of different nickel phosphide-based HER electrocatalysts.

Electrocatalyst	Substrate	Morphology	Overpotential [mV]			Tafel slope [mV dec^{-1}]	Ref.
			η_{10}	η_{100}	$\Delta\eta_{100-10}$		
NiP_2	Carbon cloth	Nanosheet	134	203.5	69.5	67	[41]
Mn-doped NiP_2	Carbon cloth	Nanosheet	97	–	–	61	[42]
Fe-doped NiP_2	Carbon paper	Nanoparticle	250	–	–	72.2	[33]
Se-doped NiP_2	Carbon cloth	Nanoflake	119	219.6	100.6	81	[34]
Ni_2P	–	Nanosheet	110	360	250	43	[35]
Ni_2P/N-doped carbon	Nickel foam	Nanoparticle	84	–	76	106	[43]
Mn-doped Ni_2P	Nickel foam	Nanosheet	–	205	–	71.8	[36]
V-doped Ni_2P	Carbon cloth	Nanosheet	85	–	–	95	[44]
Mo-doped Ni_2P	Nickel foam	Nanowire	78	–	–	109	[45]
S-doped Ni_2P	Nickel foam	Nanosheet	87.5	–	–	62.1	[46]
Ni_5P_4	Nickel foam	Nanoparticle	64	295.9	231.9	64	[47]
Ni_5P_4	–	Nanosheet	147	–	–	56	[37]
Ni_5P_4	Carbon cloth	Nanosheet	93	167	74	58.2	[48]
V-doped Ni_5P_4	Nickel foam	Nanosheet	13	–	–	–	[49]
Fe-doped Ni_5P_4	Carbon paper	Nanosheet	94.5	194.4	99.9	91	[38]
N-doped Ni_5P_4	–	Sphere	96	186.8	90.8	62.2	[39]
S-doped Ni_5P_4	Nickel foam	Nanoparticle	103	–	–	–	[50]
20% Co-doped Ni_5P_4	Carbon cloth	Nanosheet	100.5	176.8	76.3	65.8	this work

Note: 1)The '–' in the substrate column represents the form of the electrocatalyst as a powder, which is tested on a glassy carbon electrode; 2) The electrolyte used in all listed experiments is 1.0 m KOH.

Nyquist plots of 20% Co-doped Ni_5P_4, 10% Fe-doped Ni_5P_4, 20% Cu-doped Ni_5P_4, and Ni_5P_4 nanosheets. The equivalent circuit applied in the EIS fitting is shown in Figure S9, Supporting Information. All electrocatalysts demonstrate the small solution resistance ($R_s < 2\ \Omega$), indicating the reliable contact between electrocatalysts and CC substrates. As a key parameter to describe the electrocatalytic kinetics toward HER, the R_{ct} values of 20% Co-doped Ni_5P_4, 10% Fe-doped Ni_5P_4, 20% Cu-doped Ni_5P_4, and Ni_5P_4 nanosheets are found to be 27.6, 145.4, 189.7, and 218.5 Ω, respectively. The smallest R_{ct} value indicates that a faster electron transfer process is occurred in 20% Co-doped Ni_5P_4 nanosheets at the catalyst/electrolyte interface, contributing to the enhanced catalytic performance.[51] In the practical use of HER, apart from electrocatalytic activity, the stability is another important parameter for the evaluation of an efficient electrocatalyst. To investigate the cycling stability of 20% Co-doped Ni_5P_4 nanosheets, the continuous CV test is performed from −1.0 to −1.8 V (vs Ag/AgCl) at a scan rate of 100 mV s^{-1} as shown in Figure 2e. It displays a negligible change of 9.5% in η_{10} and unchanged overpotential in η_{100} after 2000 cycles. The durability of electrocatalysts is also characterized by continuous electrolysis for 24 h under a fixed current density of 10 mA cm^{-2} (Figure 2f). Evidently, this insignificant overpotential change from 108.2 to 137.2 mV presents an excellent stability, which has consequent prospects for practical electrochemical applications. In short, with the proper d-band center positioning, the improved HER performance of ultra-thin Ni_5P_4 nanosheets can be simply achieved by doping with the suitable kind and optimal amount of heteroatoms.

Moreover, the morphology, crystallinity, chemical composition, and other physical properties of ultra-thin Co-doped Ni_5P_4 nanosheets are thoroughly evaluated. It is clear that the as-prepared electrocatalysts have a uniform nanosheet morphology fully covered on the CC substrate (Figure S10a–c, Supporting Information). The detailed morphologies of the precursor of 20% Co-doped Ni_5P_4, the electrocatalysts of Ni_5P_4 and 20% Co-doped Ni_5P_4 after phosphorization are shown in **Figure 3**a–c. The precursor of 20% Co-doped Ni_5P_4 prepared by a facile solvothermal process exhibits ultra-thin 2D nanosheet morphology with the size of 0.5–1.0 µm. After annealing, the 2D nanosheet morphologies of Ni_5P_4 and 20% Co-doped Ni_5P_4 are maintained (Figure 3b,c). Simultaneously, apparent nano-sized pores appear on the nanosheets, which is due to the decomposition of hydroxide precursors during annealing, possibly contributing to an increased number of active sites. The morphology of nanosheets and nano-sized pores are also observed by transmission electron microscopy (TEM). As presented in Figure 3d,e, pores with the size of 5–10 nm distribute randomly on the 20% Co-doped Ni_5P_4 nanosheet. Such morphology can help to release the abundant active surface and therefore speed up the kinetics of the catalytic reaction.[52] Lattice spacings of 0.175 and 0.308 nm (Figure 3f), observed by high-resolution TEM (HRTEM), can be
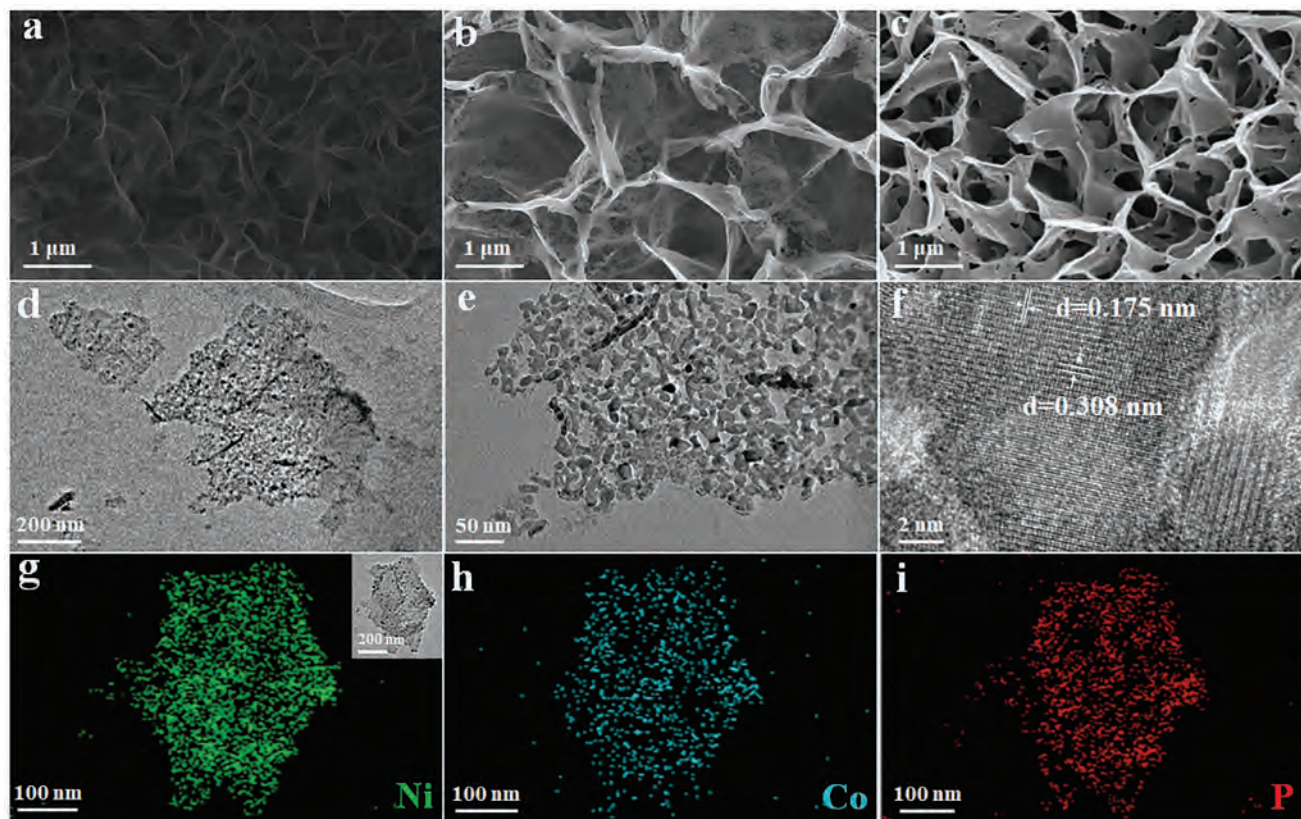
Figure 3. Morphology, crystal structure, and chemical composition of Ni_5P_4 nanosheets with the tunable d-band center. SEM images of a) precursor of 20% Co-doped Ni_5P_4 nanosheets, b) Ni_5P_4 nanosheets, and c) 20% Co-doped Ni_5P_4 nanosheets. d–f) TEM and HRTEM images of 20% Co-doped Ni_5P_4 nanosheets. g–i) EDS mappings of 20% Co-doped Ni_5P_4 nanosheets.

assigned to (106) and (103) planes of Ni_5P_4. In addition, energy-dispersive X-ray spectroscopy (EDS) mappings display the homogeneous distribution of Ni, Co, and P (Figure 3g–i) and the molar ratio of Co/(Ni + Co) is 0.19:1. Meanwhile, inductively coupled plasma-optical emission spectrometry (ICP-OES) is employed to assess the accurate information of composition, which shows the molar ratio of (Ni + Co)/P for Ni_5P_4 and 20% Co-doped Ni_5P_4 being 1.23:1 and 1.19:1, respectively (Table S1, Supporting Information). Furthermore, X-ray diffraction (XRD) is adopted for checking the crystal phase of the as-prepared precursors and Ni_5P_4-based nanosheets. As shown in Figure S11, Supporting Information, all the peaks observed in XRD patterns of precursors can be indexed to $Ni_3(NO_3)_2(OH)_4$ of hexagonal structure (JCPDS No: 22-0752).[27] After the phosphating process, all the peaks in the formers can be indexed to Ni_5P_4 of hexagonal structure (JCPDS-18-0883).[38] From the observations, the heteroatoms doping will cause a peak shift (from 40.68° (pure Ni_5P_4) to 40.84° (20% Co-doped Ni_5P_4), to 40.7° (10% Fe-doped Ni_5P_4), and to 40.84° (20% Cu-doped Ni_5P_4)). These positive shifts of XRD peaks indicate the success doping of Co, Fe, and Cu into the electrocatalysts.[53] Besides, the heteroatoms doping makes several characteristic peaks disappeared, especially for the peaks around 30° and 55°, which means more crystal defects are introduced. These defects will be benefit to the performance enhancement of electrocatalysts.[24] This result is consistent with previously published electrocatalyst studies.[14] It is worth to pointing out that the peak shift is related to the doping level. With a low-level doping, the peak shift will be difficult to be observed in XRD patterns due to small change of lattice parameter. In this case, with the 2D nanosheet morphology, nano-sized pores, and controlled Co-doping, ultra-thin Ni_5P_4

nanosheets with enhanced HER performance can be readily obtained by a solvothermal method, followed by a CVD phosphorization process.

Ultraviolet photoelectron spectroscopy (UPS) is next employed to further verify the downshift of the d-band center position of nanosheets. As shown in **Figure 4**a, the maximum values of the valence band of Ni_5P_4 and 20% Co-doped Ni_5P_4 nanosheets are nearly 4.37 and 4.40 eV, respectively. This finding indicates that the valence band is shifted away from the Fermi level after Co doping and a decrease in DOS related to the Fermi energy level.[54] Because of the valence electrons close to Fermi level relative to the d states, such a downshifted d-band center mentioned above could be attributed to the change of valence band after Co doping.[55] Furthermore, X-ray photoelectron spectroscopy (XPS) is also exploited to study the surface composition and electronic state of active electrocatalysts. As shown in Figure S12, Supporting Information, the survey spectrum of the 20% Co-doped Ni_5P_4 nanosheets reveals the coexistence of Ni, Co, and P elements, while the spectrum of Ni_5P_4 nanosheets only presents the coexistence of Ni and P elements. And the surface molar ratio of Co/(Ni + Co) of 20% Co-doped Ni_5P_4 is 0.21:1. This observation is in accordance with the results of EDS and ICP-OES. Compared to Co 2p spectra of Ni_5P_4 nanosheets, there are obvious binding peaks in 20% Co-doped Ni_5P_4 nanosheets, indicating the success of Co doping in Ni_5P_4 nanosheets (Figure 4b). In the Co 2p spectra of 20% Co-doped Ni_5P_4 nanosheets, the peaks located at 778.3, 781.5, and 785.2 eV are the Co $2p_{3/2}$ binding energies of Co—P, Co—O due to air oxidation, and satellite peak, respectively. In the Ni 2p spectra of 20% Co-doped Ni_5P_4 nanosheets (Figure 4c), the peaks located at 853.2, 856.6, and 861.9 eV are associated with the typical Ni $2p_{3/2}$ binding energies of Ni—P
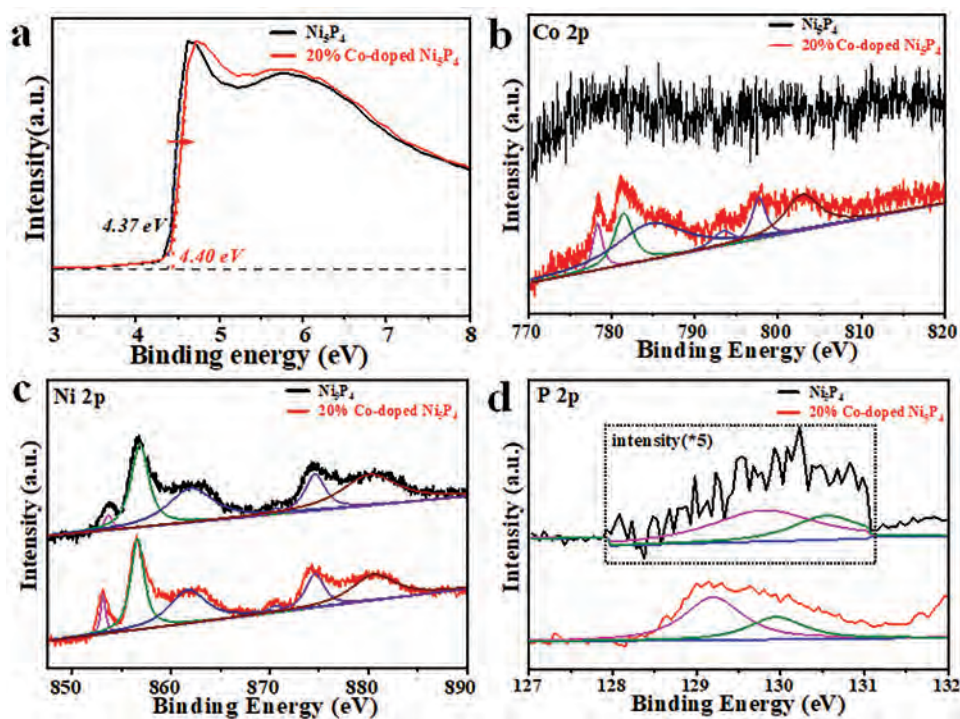
Figure 4. Surface state of ultra-thin Ni_5P_4 nanosheets with the tunable d-band center. a) UPS spectra of Ni_5P_4 and 20% Co-doped Ni_5P_4. High-resolution XPS spectra of b) Co 2p, c) Ni 2p, and d) P 2p.

bond in Ni_5P_4, Ni—O bond (due to air oxidation) and satellite peak, respectively.[39] In the P 2p spectra of 20% Co-doped Ni_5P_4 (Figure 4d), the peaks located at 129.2 and 129.9 eV are associated with the typical P $2p_{3/2}$ and P $2p_{1/2}$, accordingly.[38] Notably, the Ni $2p_{3/2}$ peak shifts positively from that of metallic Ni (852.3 eV) to 853.2 eV, whereas the P $2p_{3/2}$ peak of Ni_5P_4 shifts negatively from that of elemental P (129.9 eV) to 129.2 eV. This result indicates that Ni of Ni_5P_4 possesses a partial positive charge, whereas P possesses a partial negative charge, suggesting the electron transfer from Ni to P.[49] Meanwhile, compared to Ni $2p_{3/2}$ binding energies of Ni_5P_4 (853.6 eV), this value of 20% Co-doped Ni_5P_4 nanosheets (853.1 eV) shifts negatively, which is due to Co doping caused by the different electronegativity between Ni and Co elements.[39,49] This phenomenon can be attributed to the adsorption of hydrogen ions on these sites. This is because the sites with lower binding energies can share the electrons easily with electrophilic atoms (like hydrogen in the HER process), which can lead to the electron transfer from these sites to the adsorption of hydrogen ions.[56] Therefore, the results of UPS and XPS evidently verify the tuning effect of Co doping on the d-band center position, illustrating that Ni with the lower binding energy mainly dominates the active sites for HER.

3. Conclusion

In summary, highly HER-active ultra-thin Ni_5P_4 nanosheets with tunable d-band centers are successfully realized by heteroatom doping. DFT calculations reveal that the optimal ΔG_H value can be achieved when the d-band center is adjusted to the appropriate position (neither too high nor too low). Using an optimal Co-doping composition of 20%, ultra-thin Ni_5P_4 nanosheets show the excellent HER performance with a low overpotential of 100.5 mV at 10 mA cm^{-2} with a Tafel slope 65.8 mV dec^{-1}. Tuning the position of d-band center can improve the strength of H during adsorption/desorption processes and optimize the ΔG_H, which can contribute to the enhanced electrochemical performance. All these results can provide valuable insights into the proper design of the d-band center position of electrocatalysts by proper doping for practical hydrogen production via water splitting in alkaline media.

4. Experimental Section

Preparation of Co/Fe/Cu-Doped Ultra-Thin Nickel Hydroxide Precursors and Nanosheets: All the chemical reagents were analytical grade and used without any further purification. Co-doped nickel hydroxide nanosheets were synthesized on CC through a solvothermal method. First, CC with size of 1.5 cm × 3 cm was treated by oxygen plasma exposure with an optimal power, sequentially cleaned with deionized water and ethanol for 10 min in an ultrasonic bath and dried at 60 °C in a drying oven. Then, 0.16 mmol $Ni(NO_3)_2 \cdot 6H_2O$ and 0.04 mmol $Co(NO_3)_2 \cdot 6H_2O$ were used as the raw materials for the metal ion sources and dissolved into 20 mL ethanol to form a transparent solution. After adding the pretreated CC, the transparent solution was transferred into a 25 mL Teflon-lined stainless steel autoclave and kept at 120 °C for 24 h. After cooling to room temperature naturally, the precursor grown on CC was cleaned by ethanol and dried at 60 °C in a drying oven for 2 h. As same as the preparation process mentioned above, Fe/Cu-doped nickel hydroxide nanosheets grown on CC were also synthesized, in which the dopant sources were $Fe(NO_3)_3 \cdot 9H_2O$ and $Cu(NO_3)_2 \cdot 3H_2O$.

Preparation of Co/Fe/Cu-Doped Nickel Phosphide Ultra-Thin Nanosheets: Typically, anhydrous sodium hypophosphite and a piece of as-prepared nickel hydroxide precursors were placed in two separated quartz boats, which were positioned at upstream and downstream zones, respectively. Subsequently, the adopted one-zone furnace is heated to a designed temperature for 1 h at a heating rate of 1 °C min^{-1} in Ar atmosphere. The mass loading of active 20% Co-doped Ni_5P_4 nanosheets was about 0.5 mg cm^{-2}.

Materials Characterizations: Phase formation was identified using XRD (D8 Advance, Bruker, Cu Kα radiation). Morphology was observed by a scanning electron microscope (SEM, Nova NanoSEM 450). The microstructure was analyzed by TEM (JEOL 2100F), associated with EDS. The composition was tested using ICP-OES (Agilent 5110). UPS (AXIS Supra equipped with a He discharge lamp) and XPS (PHI5000V equipped with a monochromatic Al Kα source) measurements were carried out to investigate the electronic structure and chemical state.

Electrochemical Measurements: Electrochemical measurements were performed by an electrochemical workstation (CHI 760E, Shanghai Chenhua Instrument Co., Ltd.) in a standard three-electrode system. The as-prepared ultra-thin nanosheets electrocatalysts were used as working electrodes without further treatments in the alkaline medium of 1.0 M KOH solution. Graphite electrode and a saturated Ag/AgCl electrode were used as counter and reference electrodes, respectively. LSV was performed at the scan rate of 2 mV s^{-1}. The C_{dl} was evaluated by CV curves with the scanning rates from 10 to 80 mV s^{-1} and from the slope of the plots of capacitive current versus scan rate. EIS was carried out at −0.05 V versus reverse hydrogen electrode (RHE) with a frequency range of 10^{-2} to 10^5 Hz with AC signal amplitude of 5 mV. Equivalent circuit for fitting EIS data was achieved with Zview software. The current density was normalized to the geometric area of the electrodes. Measured potentials versus Ag/AgCl (saturated solution) were converted to RHE according to the Nernst equation:

$$E_{RHE} = E_{Ag/AgCl} + 0.197 + 0.059\,pH \tag{1}$$

The stability test of electrocatalyst was performed by taking 2000 CV cycles at a scan rate of 100 mV s^{-1} from −1.0 to −1.8 V versus Ag/AgCl, and then again LSV was measured with the same condition as the initial one. The stability was also performed by the chronopotentiometry measurements at a fixed current density of 10 mA cm^{-2} for 24 h.

DFT Calculations: First-principles calculations were carried out by using the Vienna Ab initio Simulation Package code,[57] the projected augmented wave method and the spin-polarized generalized gradient approximation[58] were used to describe the electron-core interaction and the exchange-correlation functional. DFT-D3 method[59] in Grimme's scheme was adopted to describe the van der Waals interactions. The electron wave functions were expanded in a plane-wave basis set with cutoff energy of 450 eV. And the convergence tolerances of energy and force were set to be 1×10^{-4} eV and 0.02 eV Å^{-1}, respectively. To eliminate the interaction between adjacent periodic units, more than 20 Å vacuum space in the z-direction was added. A $2 \times 3 \times 1$ gamma-centered Monkhorst–Pack k-mesh was used for geometry optimization. The Gibbs free energy calculation for the adsorption of H atoms was assessed with computational hydrogen electrode model,[60] which can be obtained by the following expression:

$$\Delta G_H = \Delta E_H + \Delta E_{ZPE} - T\Delta S_H \tag{2}$$

where ΔE_H is the hydrogen adsorption energy, ΔE_{ZPE} and ΔS_H refer to the changes of zero-point energy and entropy between the adsorbed state and the gas phase H_2, respectively. T is the temperature (298.15 K is adopted in this work), and the entropies of the free molecule come from the NIST database.

Supporting Information

Supporting Information is available from the Wiley Online Library or from the author.

[1] E. Samuel, B. Joshi, M.-W. Kim, M. T. Swihart, S. S. Yoon, *Nano Energy* **2020**, *72*, 104648.

[2] A. I. Inamdar, H. S. Chavan, B. Hou, C. H. Lee, S. U. Lee, S. Cha, H. Kim, H. Im, *Small* **2020**, *16*, 1905884.

[3] W. Zhang, R. Li, H. Zheng, J. Bao, Y. Tang, K. Zhou, *Adv. Funct. Mater.* **2021**, *31*, 202009057.

[4] M. Nemiwal, T. C. Zhang, D. Kumar, *Int. J. Hydrogen Energy* **2021**, *46*, 21401.

[5] J. M. Barlow, J. W. Ziller, J. Y. Yang, *ACS Catal.* **2021**, *11*, 8155.

[6] R. Kumar, A. Gaur, T. Maruyama, C. Bera, V. Bagchi, *ACS Appl. Mater. Interfaces* **2020**, *12*, 57898.

[7] C. C. Miao, X. W. Zheng, J. M. Sun, H. Wang, J. Qiao, N. Han, S. P. Wang, W. Gao, X. H. Liu, Z. X. Yang, *ACS Appl. Energy Mater.* **2021**, *4*, 927.

[8] Y. J. Tang, H. Zheng, Y. Wang, K. Zhou, *Adv. Funct. Mater.* **2021**, *31*, 202102648.

[9] P. P. Sun, D. R. Kripalani, K. Zhou, *Phys. Chem. Chem. Phys.* **2020**, *22*, 700.

[10] M. Das, N. Jena, T. Purkait, N. Kamboj, A. De Sarkar, R. S. Dey, *J. Mater. Chem. A* **2019**, *7*, 23989.

[11] M. Ledendecker, J. S. Mondschein, O. Kasian, S. Geiger, D. Gohl, M. Schalenbach, A. Zeradjanin, S. Cherevko, R. E. Schaak, K. Mayrhofer, *Angew. Chem., Int. Ed.* **2017**, *56*, 9767.

[12] Y. Zhao, J. Zhang, Y. Xie, B. Sun, J. Jiang, W. J. Jiang, S. Xi, H. Y. Yang, K. Yan, S. Wang, X. Guo, P. Li, Z. Han, X. Lu, H. Liu, G. Wang, *Nano Lett.* **2021**, *21*, 823.

[13] I. K. Mishra, H. Q. Zhou, J. Y. Sun, K. Dahal, Z. S. Ren, R. He, S. Chen, Z. F. Ren, *Mater. Today Phys.* **2018**, *4*, 1.

[14] C. Miao, T. Zhang, F. Li, L. Zhang, J. Sun, D. Liu, L. Wu, H. Wang, F. Chen, L. He, N. Han, Y. Ma, Y. Dai, Z. X. Yang, *Nanotechnology* **2021**, *32*, 265402.

[15] D. Q. Gao, J. Y. Zhang, T. T. Wang, W. Xiao, K. Tao, D. S. Xue, J. Ding, *J. Mater. Chem. A* **2016**, *4*, 17363.

[16] D. Yang, Z. Su, Y. Chen, K. Srinivas, J. Gao, W. Zhang, Z. Wang, H. Lin, *Small* **2021**, *17*, 2006881.

[17] J. Y. Zhang, X. W. Bai, T. T. Wang, W. Xiao, P. P. Xi, J. L. Wang, D. Q. Gao, J. Wang, *N.-M. Lett.* **2019**, *11*, 2.

[18] Y. M. Wang, G. F. Qian, Q. L. Xu, H. Zhang, F. Shen, L. Luo, S. B. Yin, *Appl. Catal., B.* **2021**, *286*, 119881.

[19] L. Z. Bian, W. Gao, J. M. Sun, M. M. Han, F. L. Li, Z. F. Gao, L. Shu, N. Han, Z. X. Yang, A. M. Song, Y. Q. Qu, J. C. Ho, *ChemCatChem* **2018**, *10*, 1571.

[20] Z. Chen, Y. Song, J. Cai, X. Zheng, D. Han, Y. Wu, Y. Zang, S. Niu, Y. Liu, J. Zhu, X. Liu, G. Wang, *Angew. Chem., Int. Ed.* **2018**, *57*, 5076.

[21] C. Tsai, K. Chan, J. K. Norskov, F. Abild-Pedersen, *J. Phys. Chem. Lett.* **2014**, *5*, 3884.

[22] C. Liu, H. Li, J. Chen, Z. Yu, Q. Ru, S. Li, G. Henkelman, L. Wei, Y. Chen, *Small* **2021**, *17*, 2007249.

[23] C. Zhang, X. Liang, R. N. A. Xu, C. N. Dai, B. Wu, G. Q. Yu, B. H. Chen, X. L. Wang, N. Liu, *Adv. Funct. Mater.* **2021**, *31*, 2008298.

[24] Y. Ma, M. Chen, H. Geng, H. Dong, P. Wu, X. Li, G. Guan, T. Wang, *Adv. Funct. Mater.* **2020**, *30*, 2000561.

[25] C. Hegde, X. Sun, K. N. Dinh, A. Huang, H. Ren, B. Li, R. Dangol, C. Liu, Z. Wang, Q. Yan, H. Li, *ACS Appl. Mater. Interfaces* **2020**, *12*, 2380.

[26] Y. Lin, K. Sun, X. Chen, C. Chen, Y. Pan, X. Li, J. Zhang, *J. Energy Chem.* **2021**, *55*, 92.

[27] Z.-X. Yang, W. Zhong, C. Au, J.-Y. Wang, Y.-W. Du, *CrystEngComm* **2011**, *13*, 1831.

[28] M. Ledendecker, S. K. Calderon, C. Papp, H. P. Steinruck, M. Antonietti, M. Shalom, *Angew. Chem., Int. Ed.* **2015**, *54*, 12361.

[29] C. Wei, Y. Sun, G. G. Scherer, A. C. Fisher, M. Sherburne, J. W. Ager, Z. J. Xu, *J. Am. Chem. Soc.* **2020**, *142*, 7765.

[30] L. L. Huo, B. C. Liu, Z. Q. Gao, J. Zhang, *J. Mater. Chem. A* **2017**, *5*, 18494.

[31] X. F. Lu, L. Yu, X. W. D. Lou, *Sci. Adv.* **2019**, *5*, eaav6009.

[32] H. Jin, S. Liu, L. Pei, G. Li, Z. F. Ma, W. F. Bai, S. T. Wu, Y. J. Yuan, J. S. Zhong, *RSC Adv.* **2021**, *11*, 22467.

[33] J. D. Costa, J. L. Lado, E. Carbó-Argibay, E. Paz, J. Gallo, M. F. Cerqueira, C. Rodríguez-Abreu, K. Kovnir, Y. V. Kolen'ko, *J. Phys. Chem. C* **2016**, *120*, 16537.

[34] Y.-C. Chu, C.-J. Chang, Y. Zhu, S.-C. Lin, C.-W. Tung, T.-L. Chen, H. M. Chen, *ACS Sustainable Chem. Eng.* **2019**, *7*, 14247.

[35] U. P. Suryawanshi, U. V. Ghorpade, D. M. Lee, M. R. He, S. W. Shin, P. V. Kumar, J. S. Jang, H. R. Jung, M. P. Suryawanshi, J. H. Kim, *Chem. Mater.* **2021**, *33*, 234.

[36] P. M. Xu, L. J. Qiu, L. C. Wei, Y. Y. Liu, D. S. Yuan, Y. Wang, P. Tsiakaras, *Catal. Today* **2020**, *355*, 815.

[37] S. Lai, C. Lv, S. Chen, P. Lu, X. She, L. Wan, H. Wang, J. Sun, D. Yang, X. Zhao, *J. Alloys Compd.* **2020**, *817*, 152727.

[38] J. Qi, T. Xu, J. Cao, S. Guo, Z. Zhong, J. Feng, *Nanoscale* **2020**, *12*, 6204.

[39] G. Y. Zhou, Y. R. Ma, X. M. Wu, Y. Z. Lin, H. Pang, M. Y. Zhang, L. Xu, Z. Q. Tian, Y. W. Tang, *Chem. Eng. J.* **2020**, *402*, 126302.

[40] Y. N. Men, P. Li, J. H. Zhou, G. Z. Cheng, S. L. Chen, W. Luo, *ACS Catal.* **2019**, *9*, 3744.

[41] Q. Fu, X. Wang, J. Han, J. Zhong, T. Zhang, T. Yao, C. Xu, T. Gao, S. Xi, C. Liang, L. Xu, P. Xu, B. Song, *Angew. Chem., Int. Ed.* **2021**, *60*, 259.

[42] X. D. Wang, H. P. Zhou, D. K. Zhang, M. Y. Pi, J. J. Feng, S. J. Chen, *J. Power Sources* **2018**, *387*, 1.

[43] X. W. Lv, Z. P. Hu, L. Chen, J. T. Ren, Y. P. Liu, Z. Y. Yuan, *ACS Sustainable Chem. Eng.* **2019**, *7*, 12770.

[44] L. L. Wen, J. Yu, C. C. Xing, D. L. Liu, X. J. Lyu, W. P. Cai, X. Y. Li, *Nanoscale* **2019**, *11*, 4198.

[45] Y. Q. Sun, L. F. Hang, Q. Shen, T. Zhang, H. L. Li, X. M. Zhang, X. J. Lyu, Y. Li, *Nanoscale* **2017**, *9*, 16674.

[46] L. L. D. Thi, P. N. K. Tuyen, T. Y. Vu, *Nanotechnology* **2020**, *31*, 465401.

[47] C. Lai, X. Liu, Y. Deng, H. Yang, H. Jiang, Z. Xiao, T. Liang, *Inorg. Chem. Commun.* **2018**, *97*, 98.

[48] A. Y. Chen, L. Fu, W. J. Xiang, W. Wei, D. Liu, C. L. Liu, *Int. J. Hydrogen Energy* **2021**, *46*, 11701.

[49] Y. Rao, S. Wang, R. Zhang, S. Jiang, S. Chen, Y. Yu, S. Bao, M. Xu, Q. Yue, H. Xin, Y. Kang, *ACS Appl. Mater. Interfaces* **2020**, *12*, 37092.

[50] Y. Lin, Y. Pan, J. Zhang, *ChemElectroChem* **2017**, *4*, 1108.

[51] W. J. He, L. L. Han, Q. Y. Hao, X. R. Zheng, Y. Li, J. Zhang, C. C. Liu, H. Liu, H. L. L. Xin, *ACS Energy Lett.* **2019**, *4*, 2905.

[52] M. Zhang, J. Wang, Y. Zhang, L. Ye, Y. Gong, *Dalton Trans.* **2021**, *50*, 2973.

[53] C. F. Li, J. W. Zhao, L. J. Xie, J. Q. Wu, G. R. Li, *Appl. Catal., B* **2021**, *291*, 119987.

[54] M. T. Gorzkowski, A. Lewera, *J. Phys. Chem. C* **2015**, *119*, 18389.

[55] L. Wang, Z. J. Li, K. X. Wang, Q. Z. Dai, C. J. Lei, B. Yang, Q. H. Zhang, L. C. Lei, M. K. H. Leung, Y. Hou, *Nano Energy* **2020**, *74*, 104850.

[56] N. Masurkar, N. K. Thangavel, L. M. R. Arava, *ACS Appl. Mater. Interfaces* **2018**, *10*, 27771.

[57] G. Kresse, *Phys. Rev. B* **1996**, *54*, 11169.

[58] P. P. John, K. Burke, M. Ernzerhof, *Phys. Rev. Lett.* **1996**, *77*, 1787.

[59] S. Grimme, *J. Comput. Chem.* **2006**, *27*, 1787.

[60] J. K. Nørskov, J. Rossmeisl, A. Logadottir, L. Lindqvist, *J. Phys. Chem. B* **2004**, *108*, 17886.